PHYSICAL REVIEW B **109**, 245430 (2024)

Transport characteristics of epitaxial graphene proximitized to a two-dimensional Pb interface layer

Markus Gruschwitz,[1] Tim Güldenpfennig,[1] Andreas Cordier,[1] Chitran Ghosal,[1]
Sergii Sologub,[1,2] and Christoph Tegenkamp[1,*]
[1]*Analytik an Festkörperoberflächen, Institut für Physik, Technische Universität Chemnitz, Reichenhainer Str. 70, 09126 Chemnitz, Germany*
[2]*Institute of Physics, National Academy of Sciences of Ukraine, Nauki Avenue 46, 03028 Kyiv, Ukraine*

(Received 13 February 2024; revised 20 April 2024; accepted 13 June 2024; published 26 June 2024)

Proximity coupling is an intriguing quantum concept to tune the properties of 2D materials, e.g., graphene. By intercalation of a Pb monolayer, a 2D heterostructure of charge-neutral graphene and a crystalline 2D Pb layer on SiC(0001) substrates was epitaxially grown. Thereby, microscopy revealed characteristic defects on microscopic and mesoscopic length scales, e.g., grain boundaries, substrate steps, and nonintercalated terraces. We analyzed *in situ* the electronic transport properties of this heterostructure. The systematic variation of the contact geometry and probe spacings, supplemented by finite-element simulations, allowed us to circumvent the problem of sample inhomogeneities and to determine reliably the conductivity of the 2D heterostructure itself. Thereby, the conductivity of $(7 \pm 1) \times 10^5$ S/m is comparable to values measured for monolayer and quasi-free monolayer graphene, but decreases with decreasing temperature down to 30 K, revealing a clear nonmetallic behavior. Our findings are compatible with a small gap opening (1–5 meV) in graphene due to the proximitized 2D Pb layer.

DOI: 10.1103/PhysRevB.109.245430

I. INTRODUCTION

Extensive research has been conducted in the past to investigate and further tune the exceptional properties of graphene [1,2]. A noteworthy frontier involves the coupling of various two-dimensional (2D) materials to create superconducting graphene and other novel quantum materials by proximity coupling [3].

A promising way to achieve this is through the intercalation of the graphene layer with various elements. Regarding the decoupling of graphene from SiC(0001) substrates, various intercalants have been proven to be suitable in forming (partly) well-defined interface structures with different functionalities [4]. For example, intercalation of hydrogen leads to a complete saturation of the dangling bonds at the interface, thereby significantly reducing the intrinsic strong n-type doping and improving charge carrier mobilities. The residual p-type doping is an effect of the polarization of the SiC surface [5–7]. In contrast, electronic correlation effects were reported upon strong doping, e.g., due to Ca, Gd, or Yb, opening the potential for unconventional superconductivity [8–12].

Recently, the intercalation of Pb came into the focus of research [13–22]. Most interestingly, the relaxed 2D Pb-monolayer structure reveals a quasi-tenfold periodicity with respect to graphene due to the formation of a grain boundary network. The densely packed Pb monolayer efficiently minimizes the doping influenced both from the surface dangling bonds and the SiC surface polarization, giving rise to charge-neutral monolayer graphene [21]. For similar Pb-monolayer structures on Si(111), indeed, new spin-orbit coupled phases and even superconductive behavior were found [23–25]. The extent to which this can be transferred to graphene is still unknown. Epitaxially grown graphene on Pb/Pt(111) substrates revealed a strong spin-orbit gap of 200 meV at the K point of graphene [26]. However, the transfer of spin-orbit coupling mechanisms depends sensitively on microscopic details, e.g., the interlayer distance [27,28].

Particularly for the heavier elements from the periodic table, the intercalation process is complex, accompanied by multiple barriers [20]. Therefore, buffer layer samples with defects are beneficial, e.g., obtained by mild sputtering prior to intercalation [17]. In contrast, on polymer-assisted grown samples, where the formation of SiC step bunches is strongly suppressed and the carbon monolayers carpets the SiC steps [29], the success rate for intercalation can be extremely low. These limitations inevitably trigger the formation of sample inhomogeneities.

In general, while these types of defects are advantageous for intercalation experiments, they also represent a hurdle for transport measurements, since the probe currents are spreading out and sensing contributions from defects. While for homogeneous samples, the correction factors even for anisotropic systems in various dimensions are known [30], it is much more challenging to deduce correctly the conductivity of defective systems from the conductance. In order to account for this, simulations are mandatory, e.g., finite-element simulations, which can be reliably applied on mesoscopic scales for diffusive transport systems.

In this paper, we determined the conductivity of an intercalated Pb monolayer underneath graphene using an *in situ* nanoprobe technique complemented by simulations. By varying the probe spacings, the probe geometries and the substrate temperature, we were able to determine the conductivity of

---

[*] Contact author: christoph.tegenkamp@physik.tu-chemnitz.de

the terraces hosting the 2D heterostructure. The finite-element simulations showed that the steps act as barriers with a conductivity of 175 S/m at room temperature, which drops down to 15 S/m at 30 K. Moreover, by means of this combined approach of measurements and simulations, using (almost) real structures, we were able to clarify the role of defects on microscopic and mesoscopic scales. Thereby, in contrast to epitaxial monolayer graphene, the resistivity of the terraces increased, clearly showing a nonmetallic behavior for the 2D heterostructure. The analysis of the data revealed a small gap not exceeding 5 meV, which seems to be induced by spin-orbit coupling of the 2D Pb layer.

II. MATERIALS AND METHODS

The buffer layer (BL) samples were prepared from 500-μm thick, nitrogen n-type doped 4H-SiC(0001) (N dopant concentration $\approx 10^{17}$ cm^{-3}) substrates (Cree) with a miscut angle of 0.1°. Wet chemical etching followed by hydrogen etching in a 1000 hPa hydrogen atmosphere at 1425 °C for 15 min provides a clean SiC surface. Annealing this surface at 1475 °C in a 10^5 Pa Ar-atmosphere yields high quality BL terraces with an average width of 3.75 μm. The epitaxial grown BL forms a characteristic $(6\sqrt{3} \times 6\sqrt{3})$ reconstruction.

The BL was intercalated by repeated cycles of depositing Pb (Aldrich, 99.999%) from a Knudsen cell and annealing the sample by DC heating. In detail, the preparation was as follows: deposition of five monolayers (ML) Pb on the BL sample at room temperature; annealing at 770 K for 5 min; four cycles of 5 ML deposition and annealing at 770 K for 5 min twice followed by a 970 K 5-min annealing step; after depositing 21 ML and heating at 770 K for 5 min the intercalation spots reached a comparable intensity as the (6×6) reconstruction spots. Another 21 ML deposition followed by long time, mild annealing at 570 K yields intense interface spots as well as significantly increased graphene (1×1) spots. Remaining Pb clusters on the surface were inspected afterwards by scanning electron microscopy (SEM) and subsequently desorbed by annealing cycles at 670 K. This ensures an as homogeneous intercalation phase as possible. Cross-sectional scanning transmission electron microscopy (STEM) measurements were performed and knock-on damages were minimized by using low voltages and beam currents (80 kV, 120 pA) for dark-field images. The lamella was prepared with a FIB system, revealing after lift-out and subsequent thinning with Ga ions (2 kV, 30 pA) a thickness below 50 nm. Energy dispersive x-ray spectroscopy (EDS) spectra where measured at 7.5 nA probe current by integrating C-Kα, Si-Kα, and Pb-Mα emissions. Structural investigations of the surfaces and interfaces were carried out by spot profile analysis of low-energy electron diffraction (SPA-LEED), SEM as well as scanning tunneling microscopy (STM). Electronic *in situ* transport measurements were performed using a four tip STM (4pp-STM/SEM) with various probe spacings and geometries [30].

The transport measurements were supported by finite-element simulations using the software package of COMSOL Multiphysics. The structure was modeled by a 400 μm by 140 μm sheet of 0.65-nm thickness and terrace conductivity σ_T. The defects resembling the steps between terraces are introduced as a periodic array of stripes of 0.1-μm width with a barrier conductivity σ_B. The conductivity outside of our model structure was set to zero. The experimental probe setup was implemented in our simulations by four contact areas. By arranging these defined areas accordingly, both, collinear and square four-tip geometries were realized. Two of the four were biased by 1 V with respect to a 0 V reference potential. The current was calculated by integrating the normal current density component along the boundary of the applied potential area. The resistance measured in the four-tip experiment is calculated by the potential drop between the remaining two areas divided by the current.

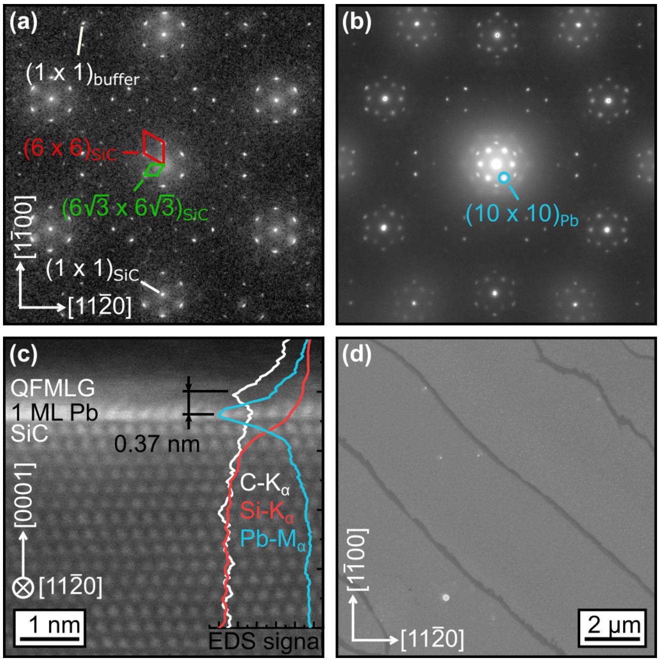

FIG. 1. (a) SPA-LEED pattern of the BL sample before intercalation. The main spots and characteristic reconstructions are indicated. (b) SPA-LEED pattern after intercalation showing the the characteristic reconstruction spots of the quasi (10×10) periodicity (with respect to graphene) due to formation of bubbles (cf. Fig. 2 and Ref. [21]). The data were taken at room temperature at an electron energy of 169 eV. (c) STEM image and EDS scans showing the intercalation of 1 ML Pb at the interface between SiC and graphene. (d) SEM image (15 kV, 1 nA, 300 K) of the surface reveals an average terrace width of 3.75 μm. The dark contrast stems from overgrowth of the step edges by MLG.

III. RESULTS AND DISCUSSION

Before we present and discuss our transport data, first the structure of our surfaces will be discussed. The correlative microscopy of SEM and STM on various scales was extremely helpful in characterizing the step and terrace structures in detail.

A. Structural properties

Figure 1(a) shows a SPA-LEED image of the initial surface, i.e., the BL on SiC(0001). The hallmark of a successful intercalation of a monolayer of Pb is the appearance of a

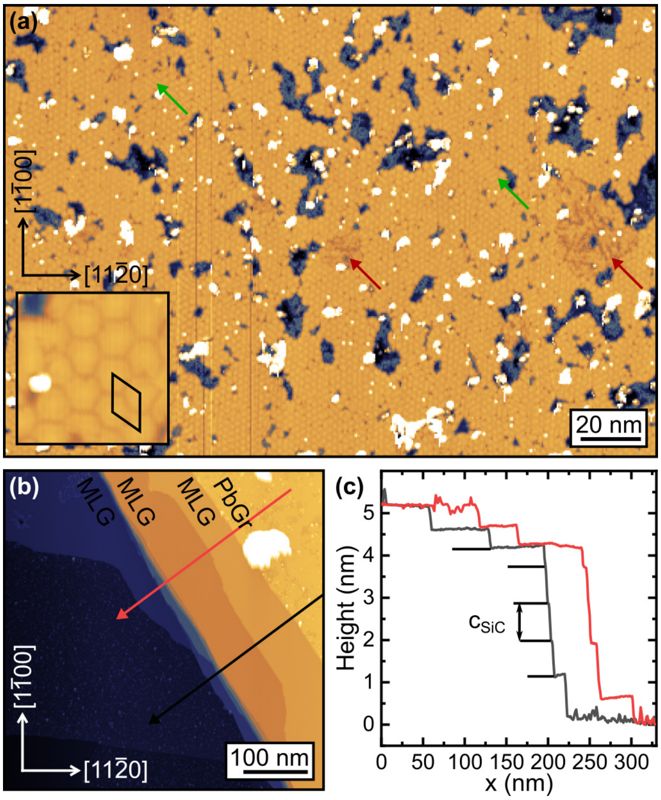

FIG. 2. (a) STM mapping (+2 V, 200 pA, LN$_2$) of an intercalated terrace. The bubble phase is percolated and dominant over BL (dark regions), an unordered phase (red arrow) and remnant striped phase (green arrow). The $10 \times 10\,\text{nm}^2$ inset reveals the local bubble-like structure. (b) STM mapping (+2 V, 200 pA) of a terrace step showing both Pb-intercalated areas (PbGr) as well as growth of MLG at the step bunches. (c) Height profile along the direction in (b) showing a accumulation of full or half unit-cell substeps each overgrown by MLG. The width of this step bunching ranges from tens of nm to several hundred nm.

quasi (10 × 10) reconstruction, seen in Fig. 1(b), which results from the periodicity of either a three-domain stripe or the bubble phases [17,18]. The increased intensity compared to the (6 × 6) spots as well as the presence of higher-order spots suggests a high-quality and extended interface reconstruction. A detailed structural model of the bubble phase is given in Ref. [21]. This is fully supported by recent STEM measurements shown in Fig. 1(c). The EDS clearly shows the formation of a ML of Pb at the interface between the topmost SiC layer and EG. The large distance between the EG and Pb of 3.7 Å is obvious and supports recent x-ray standing wave (XSW) results [21]. Moreover, the local (1 × 1) symmetry of the Pb becomes apparent from the STEM cross section.

The SEM image shown in Fig. 1(d) reflects a quite homogeneous intercalation process on the terraces, which are in the order of 3–4 μm in width. Moreover, the terraces are separated by dark stripes, which resemble bunches of SiC-steps and also growth of MLG patches at these sites (see below). The intercalation of Pb and other heavy elements crucially depends on the presence of defects [17]. Continuous improvement of epitaxial growth of graphene by, e.g., polymer-assisted growth (PASG) minimizes the density of defects in the extended graphene layers by providing additional carbon [29,31]. Ironically the high quality reached by this approach limits the accessibility of the BL for heavy intercalants. Contrarily, BL samples grown without the addition of polymers, reveal strong step bunches, which may act here as intercalation sites [31]. While it was demonstrated that in particular single atomic-height substrate steps as well defined SiC facets can be continuously overgrown by graphene, the large and steep steps here act as barriers, as we will show below [32,33]. Another sign of interrupted graphene growth at these steps bunches is the formation of monolayer graphene (MLG) patches, which show up as dark stripes in the SEM.

STM measurements were carried out to further characterize the intercalated terraces. Figure 2(a) shows a terrace site where approximately 90–95% of the area has been successfully intercalated. The majority of the intercalated phase reveals the so-called bubble phase (see inset; for details see Ref. [21]). In addition, striped phases (green arrows) were seen in some areas [17], as well as partly disordered patches of intercalated Pb (red arrows). Nevertheless, the Pb phase is percolated, thus providing a separate interface transport channel and triggering the formation of a charge neutral graphene layer. Bright contrast areas most likely stem from residual Pb on top and probably mark the defect sites in graphene from where intercalation started. Most of these Pb clusters can be finally removed by long-time annealing at 670 K. In Fig. 2(b) we show an STM image in the vicinity of a step. The line profile in Fig. 2(c) clearly reveals the formation of step bundles. Furthermore, the STM image shows that the growth of MLG is located at these sites, which are seen as dark stripes in the SEM images. While MLG on the terrace itself is conductive, most likely the step bunch itself is not continuously overgrown by graphene; thus these parts on the surface act as a barrier in transport experiments.

B. *In situ* surface transport measurements

1. *Collinear tip configurations*

In order to determine the conductivity of the 2D heterosystem, transport measurements were first performed in a collinear (cl) and equidistant manner. Within the field of view of the SEM, the four probes were brought into ohmic contact both in the center of a single terrace along the step direction, as shown in the inset of Fig. 3(a), as well as perpendicular to the step direction of the SiC substrate. The injected current between the outer probes was fixed to 10 μA. By varying the tip spacing s, the resistance values were measured. Figure 3(a) shows the values for both configurations $R^{cl}_{||}(s)$ and $R^{cl}_{\perp}(s)$. At small tip spacings a steep increase of the resistance is measured, while for larger spacings the resistance values are constant or decreasing. At least for the parallel configuration, only a constant range beyond 25 μm was found. Such a plateau was missing for the $R^{cl}_{\perp}(s)$ configuration.

In Fig. 3(b) we show a log-log representation of the $R^{cl}_{||}(s)$ data. At tip spacings smaller than the terrace width the resistance approaches a constant level of unrestricted 2D terrace resistance. Increasing the tip spacing revealed a range of (almost) linearly increasing resistance values resembling a (quasi) 1D behavior up to $s = 12$ μm, i.e., a contact separation of the current probes was 36 μm, which amounts to around

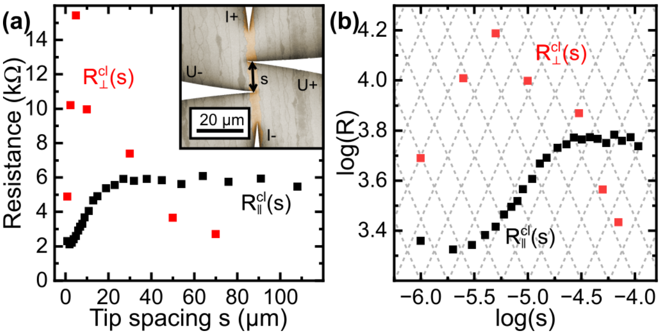

FIG. 3. (a) Tip spacing-dependent measurements of the resistance performed in a parallel configuration with respect to the steps $R^{cl}_{||}(s)$ (cf. inset), and in a perpendicular geometry $R^{cl}_{\perp}(s)$. (b) Log-log plot of $R^{cl}_{||}(s)$ and $R^{cl}_{\perp}(s)$ shown in (a) to highlight the different regimes and characteristic tip spacing dependencies. All measurements were performed at 300 K. The lines with positive and negative slopes indicate $R \propto s$ and $R \propto s^{-1}$ behaviors, respectively.

nine times the terrace width ($w_T = 4$ µm for this particular terrace). Apparently, the steps of the substrate mimic barriers with a much lower conductivity (σ_B) so that the current is confined within the terrace. Within this diffusive regime, neglecting classical edge-size effects, the resistivity of the terrace is simply given by $\rho_T = R^{cl}_{||}(s) w_T t/s$. The thickness of the graphene/Pb heterostructure is assumed to be $t = 0.65$ nm as shown by the STEM image in Fig. 1(c) and also known from x-ray standing wave experiments [21]. The conductivity at room temperature then amounts to $\sigma_T = {\rho_T}^{-1} \approx 8 \times 10^5$ S/m.

For larger tip spacings, a deviation from a 1D behavior is found, which clearly indicates a current leakage, e.g., by a finite conductivity of the barriers and/or pin holes, etc. along the step structure. As demonstrated by STM in Fig. 2(b), the step bunch height was the same everywhere. However, the less steep areas might be partly more overgrown with graphene, so that these spots may act as pin holes. Apparently, in the range from around 25 up to 100 µm this spread out compensates the 1D channel and mimics a 2D behavior, where the resistance is not dependent on the probe spacing [30]. The straightforward evaluation of this regime results in a sheet resistance of $R^{cl}_{\text{sheet}} = \rho/t \approx 2.6 \times 10^4\ \Omega/\square$ referring to a conductivity of approximately 5.7×10^4 S/m, which is at least one order of magnitude lower compared to the value derived from the 1D regime for the terraces. Apparently, here we include the resistance of the barriers and obtain an average value. As we will explain below, the contributions of the terraces and the steps can be separated from each other with the help of simulations.

Depending on the probe geometry and probe distances also a $1/s$ behavior was found, e.g., as obvious for the $R^{cl}_{\perp}$ component in the log-log plot in Fig. 3(b). For large probe distances, the resistance behavior is reminiscent of a 3D regime and similar to previous transport measurements on imperfectly intercalated graphene samples [17]. However, significant contributions from bulk transport channels, e.g., space charge layers [34], can be excluded here. The bulk resistivity of the SiC used here is at least 3–4 orders of magnitude larger [35]. Furthermore, the Fermi level pinning of both MLG and QFMLG revealed a depletion zone for the excess charge carriers [7] and previous transport measurements done on such surfaces, which underwent high-temperature annealing steps, showed no signs of parasitic doping effects [6]. Moreover, space charge effects are usually not sensitive to surface roughnesses, thus any dominant space charge layer transport should be isotropic in contrast to our findings, described in the next section. Finally, a broad spectrum of inhomogeneities such as barrier defects as well as variations in width, finite length, and different degrees of intercalation of individual terraces, lead to a considerable deviation from the locally found 1D behavior.

Qualitatively, for $R^{cl}_{\perp}(s)$ a similar trend is seen, although the quasi 2D regime, i.e., the plateau, is missing. Nevertheless, for the perpendicular configuration, the onset for the drop of the resistance is at around 3 µm, i.e., around 30 times smaller compared to the parallel configuration. The steep increase in resistance stems from addition of barriers with increasing tip spacing resembling a series connection of terraces and barriers, while in the parallel orientation the barriers only restrict the width of the channel with high conductivity. Larger tip spacings require a higher driving voltage to sustain the fixed injected current. The wide potential spread perpendicular to tip arrangement allows more defects along the terraces to lower resistance. Compared to the 2D homogeneous scenario, the current density spreads further from the voltage probes resulting in a smaller voltage drop between them. In the context of Fig. 4 we will discuss in detail the results of rotational square tip measurements, which allow a more precise study of the anisotropy.

In contrast to our findings, collinear measurements in homogeneous anisotropic 2D systems exhibit an insensitivity to the orientation of the tip assembly [30]. In this context, the increase in $R^{cl}_{\perp}(s)$ within the initial few micrometers is striking. Once the current probes extend beyond five terraces, a substantial drop in resistance occurs, aligning with the 1D/2D transition observed in the parallel direction. These transitions and the directional variability in collinear measurements are ascribed to the presence of local junctions, such as pin holes, interspersed between the terraces. The existence of these imperfections, combined with the finite resistance of the barriers and experimental constraints on the tip spacings, complicates the evaluation of the transport measurements. Consequently, we employed finite-element simulations (detailed below) in order to isolate conductivity from other contributing factors.

2. *Square tip configurations*

The effect of the steps on transport was further analyzed by using square tip arrangements (*sq*) with various tip spacings [see Fig. 4(a)]. The probes were aligned with respect to the SiC step structure, such that the current was spread out parallel ($\Theta = 0$) and perpendicular ($\Theta = \pi/2$) to the step structure. As shown in Fig. 4(b), depending on the orientation and tip spacing of the current probes relative to the step direction, the resistances $R^{sq}_{\perp}$ and $R^{sq}_{||}$ differ by more than one order of magnitude between the two configurations. Note that the data point for the perpendicular configuration at 3.5 µm was taken with all probes positioned on a single terrace, thus the values are almost identical for both modes of operation. The barriers outside the tip arrangements effectively resemble

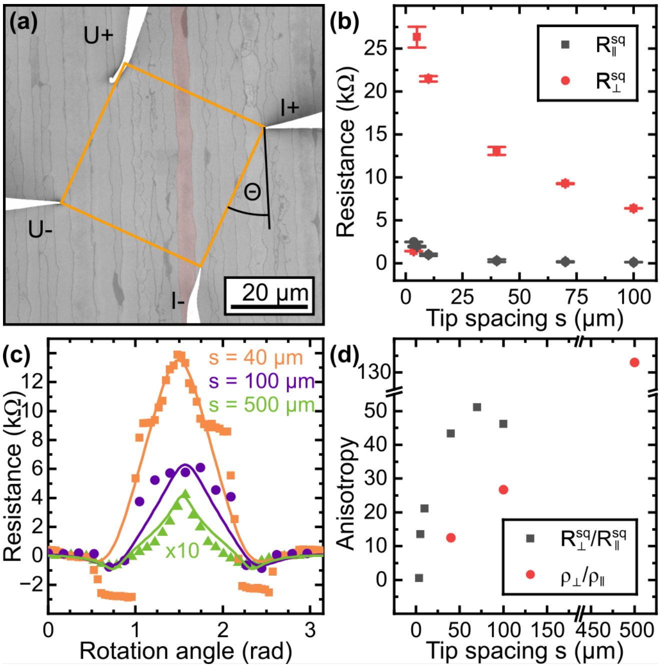

FIG. 4. (a) SEM image showing a square tip arrangement with a tip spacing of $s = 40\,\mu$m for measuring the anisotropy. The red-colored terrace was not intercalated by Pb as deduced from the SEM contrast and STM measurements. (b) Tip-distance-dependent measurements performed in a square configuration aligned parallel ($\Theta = 0$) and perpendicular ($\Theta = \pi/2$) to the step direction. The first (red) data point for the perpendicular configuration was measured on a single terrace, where the contribution of the steps is minimal. (c) Angle-dependent resistances $R(\Theta)$ measured at $40\,\mu$m (orange), $100\,\mu$m (purple), and $500\,\mu$m (green) tip spacing. Resistances measured at $500\,\mu$m are multiplied by 10 for better visibility. (d) Tip-spacing-dependent ratios, $R_{\perp}^{sq}/R_{\|}^{sq}$ and $\rho_{\perp}/\rho_{\|}$, determined from (b) and the analysis of (c), respectively. All measurements were performed at 300 K.

finite-size effects of the conductive area resulting in a smaller perpendicular resistance compared to the parallel resistance.

When the current flows along the terraces, the growing number of terraces with increasing tip spacing effectively shields the applied potential from the voltage probes, leading to a low resistance. Conversely, in a perpendicular arrangement, the less conductive barriers induce an almost stepwise potential drop between the current injection probes. The potential drop between each current injection probe and its adjacent voltage probe on the same terrace is notably lower. This distortion of the potential landscape results in an increased calculated resistance compared to the isotropic case. This distinctive form of stepwise anisotropy diverges significantly from the typically considered continuous anisotropy.

The probe-spacing-dependent ratio $R_{\perp}^{sq}/R_{\|}^{sq}$ is plotted in Fig. 4(d). The ratio increases gradually up to large tip spacings. This is an unexpected behavior if one assumes that only the terrace steps and terrace barriers are responsible for the anisotropy. Apparently, further imperfections on larger scales need to be considered, as we will show in the following.

In order to get a deeper insight, angle-resolved transport measurements were performed by gradually rotating the tip arrangement. Figure 4(c) shows the experimental results for three different tip spacings. Starting with large tip spacings, $s = 500\,\mu$m, the curve is rather smooth and almost resembles that of a homogeneous, but anisotropic surface [34,36–38]. However, the evaluation by means of the model for an homogeneous anisotropic scenario revealed a considerable deviation close to angles with two probes on one terrace ($\Theta = 0; \pi/4; \pi/2$), resulting in heavily distorted potential landscapes. At smaller tip spacings, the anisotropic curves show discontinuities and plateau-like features. For example, at $40\,\mu$m tip distance the arrangement spans across 10 to 13 terraces [see Fig. 4(a)]. The influence of the local structure feeds back to a significant deviation from comparable continuous anisotropy. For this particular case, the SEM image revealed a poorly intercalated terrace of much lower conductivity [marked in red in Fig. 4(a)]. The jumps in the resistance curve could be correlated to the positions of individual tips crossing this terrace.

Our simulations, which had to be carried out on small scales, also showed a discrete character induced due to the microscopic step barriers. Thus, the behavior in Fig. 4(c) is qualitatively supported by finite-element simulations discussed in the next subsection.

Despite the fact that our system consists of differently conductive stripes and that the distribution of these determine the anisotropy, we used the formalism derived for homogeneous anisotropic 2D systems, in order to evaluate qualitatively the (average) resistivity components [36]. The solid lines in Fig. 4(c) show the fit according to

$$R^{sq}(\Theta) = \frac{\sqrt{\rho_{\perp}\rho_{\|}}}{2\pi t} \times \ln\sqrt{\frac{\left(1+\frac{\rho_{\perp}}{\rho_{\|}}\right)^2 - 4\cos^2\Theta\sin^2\Theta\left(1-\frac{\rho_{\perp}}{\rho_{\|}}\right)^2}{\sin^2\Theta + \frac{\rho_{\|}}{\rho_{\perp}}\cos^2\Theta}}, \tag{1}$$

where $\rho_{\|}$ and $\rho_{\perp}$ denote the resistivities along ($\Theta = 0$) and perpendicular ($\Theta = \pi/2$) to the SiC step structure, respectively. The anisotropy factor $A = \rho_{\perp}/\rho_{\|}$ is shown in Fig. 4(d) as well and increases linearly with the tip spacing s.

This is a counterintuitive result. In context of Fig. 3(a) we have shown that on the mesoscopic scale, the system underwent a 1D/2D transition, most likely due to pin hole structures within the step barriers. The high anisotropy values measured for almost microscopic scales must therefore result from additional defects, e.g., nonintercalated terraces. Therefore, this mode of operation seems to be not suitable or at least not easily applicable. In order not to be influenced too much by this type of defect in our measurements, we have focused on linear tip arrangements in the following quantitative analysis.

C. Finite-element simulations

As mentioned, our system consists of at least two different conductivity regimes. An entirely 1D or 2D regime was not achieved. This mixture of 1D and 2D contributions arouse from a finite resistance of the barriers. In order to reproduce our experimental finding by finite-element-based simulations,

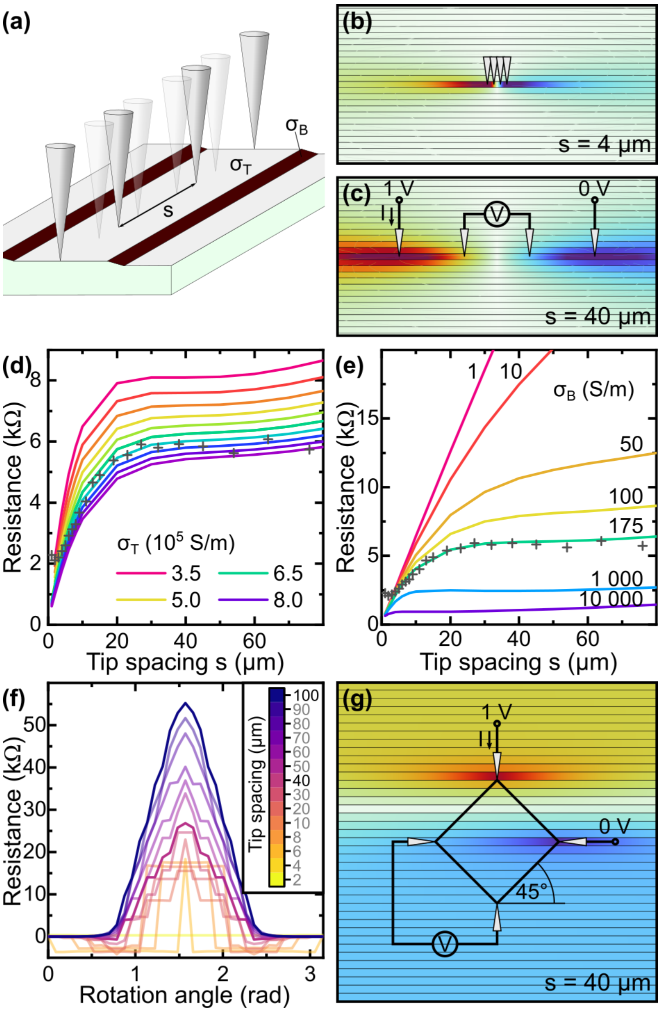

FIG. 5. (a) Microscopic model of our structure considering individual conductivities for the terrace (σ_T) and the step edge (σ_B). (b),(c) Potential distribution maps calculated for two tip spacings $s = 4\,\mu\text{m}$ and $s = 40\,\mu\text{m}$, respectively. (d) Simulated resistances $R_{||}^{cl}(s)$ for a collinear configuration as a function of the tip spacing s for different σ_T values and a constant barrier conductivity ($\sigma_B = 175\,\text{S/m}$) showing the 1D/2D transition. (e) Same as (b) but varying σ_B while keeping $\sigma_T = 6.5 \times 10^5\,\text{S/m}$ constant. The crosses in (d) and (e) refer to $R_{||}^{cl}(s)$ shown in Fig. 3(a). (f) Simulated $R^{sq}(\Theta)$ curves using a square tip arrangement and the conductivities derived from tip-distance-dependent measurements (d), (e). (g) Simulated potential distribution for a square tip arrangement with $s = 40\,\mu\text{m}$, oriented 45° with respect to the SiC step structure. The origin of negative resistance values becomes apparent in systems of strong anisotropy.

we used a simplified microscopic structure of periodic stripes with alternating conductivities, as sketched in Fig. 5(a). It consists of conductive terraces (σ_T) separated by less conductive barriers ($\sigma_B < \sigma_T$). The average widths of terraces $w_T = 3.75\,\mu\text{m}$ and barriers $w_B = 0.1\,\mu\text{m}$ were taken from high-resolution SEM mappings. Please note that this simplified model does not take any substructure or atomic details into account. Qualitatively, the above mentioned tip-spacing-dependent 1D/2D transport characteristic is already reflected in the potential distribution for different tip spacings in the collinear configuration shown in Figs. 5(b) and 5(c).

As a realistic input for our simulations, we used for the terraces the value determined from the 1D transport regime obtained for small tip spacings. Figure 5(d) shows the effect of varying the terrace conductivity σ_T for a fixed $\sigma_B = 175\,\text{S/m}$. While the curve shape remains same, mostly the slope in the 1D regime is influenced. In Fig. 5(e) the significant change of the shape of $R_{||}^{cl}(s)$ becomes apparent when σ_B was varied over several orders of magnitude at fixed $\sigma_T = 6.5 \times 10^5\,\text{S/m}$. As expected, in the limit of σ_B approaching σ_T (purple curve) we find 2D behavior for a wide range of s. As the barrier becomes less conductive, $\sigma_B \ll \sigma_T$, again the transport characteristic of a quasi-1D wire is obtained. The consistent but slight increase in resistance for tip spacings greater than 60 μm is caused by the finite-model size.

Within the transition region a quantitative agreement with our experimental data was found for barrier conductivities, which are three orders of magnitude lower than the terrace conductivity. The variation of the conductivity of both transport channel levels finally allowed us to model our experimental $R_{||}^{cl}(s)$ curve. A best agreement was achieved for $\sigma_T = 6.5 \times 10^5\,\text{S/m}$ and $\sigma_B = 175\,\text{S/m}$ with the experiment performed at 300 K. The conductivity value for the terrace, now determined from a wide range of the measured $R_{||}^{cl}(s)$, is in reasonable agreement to that value determined from the analysis of the 1D regime.

Moreover, we used these values and simulated the resistance values for the square tip assembly. The simulated $R^{sq}(\Theta)$ values as a function of the angle of the current probes with respect to the SiC step structure for different tip spacings are shown in Fig. 5(f). Exemplary, the potential distribution for a 45° square tip arrangement is shown in Fig. 5(g), highlighting the origin of negative resistances due to high anisotropy. Smooth R curves are obtained only for the largest distances that could still be realized in the simulation. The discrete microscopic structure is *invisible* for the large probe distances and, consequently, a quasi-homogeneous but anisotropic layer is measured on this scale. This changes dramatically when the probe distances become comparable with the terrace distances and the potential jumps at the steps are also reflected in the resistance curves. The measured discontinuities on the mesoscopic scale are virtually the analog of those we discussed in the context of Fig. 4(c) and the presence of nonintercalated terraces on an almost microscopic scale. Since poorly or even nonintercalated terraces exhibit further different characteristics, their influence was not included in our current modeling.

D. Temperature-dependent transport

As pointed out above, transport measurements using a square four-point arrangement on inhomogeneous (and anisotropic) samples are challenging since defects on various scales are needed to be taken into account. Therefore, we will focus in the following on collinear tip assemblies on individual terraces, performed at various temperatures. Figure 6(a) summarizes measurements at various temperatures. As obvious, the lower the temperature, the larger the tip spacing range where a quasi-1D behavior is found. The transition towards the 2D regime, which is triggered by σ_B and the defects within the barriers, is shifted to 100 μm if the temperature is

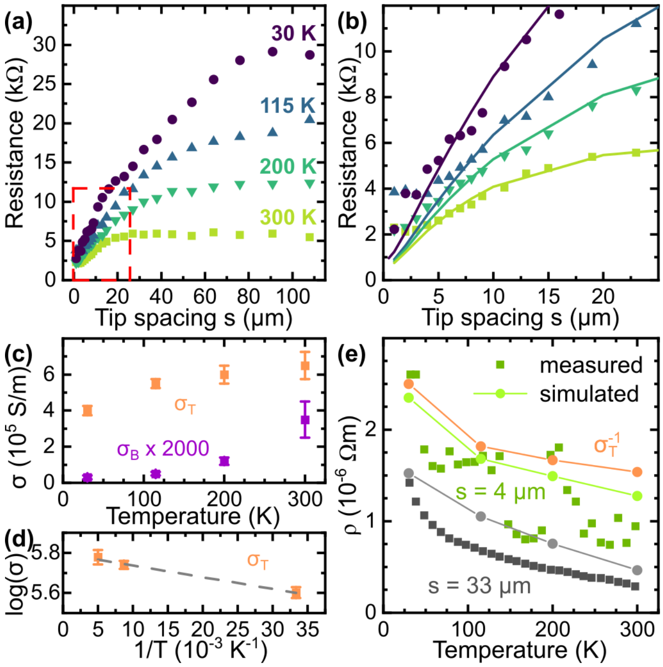

FIG. 6. (a) Collinear four-point probe measurements at 30 K, 115 K, 200 K, and 300 K, where the tips were aligned parallel to the steps. (b) Magnification of the (red-dashed) area shown in (a). The solid lines are obtained by simulations. The optimized values for σ_T and σ_B for each temperature are shown in (c). (d) Arrhenius plot and fit (dashed line) of σ_T revealing an activation energy of around 1 meV. (e) Resistivity as a function of temperature obtained from collinear four-point probe measurements at 33 μm (black square) and 4 μm (green squares). In addition, also the values obtained from R(s) measurements shown in (a) at 33 μm (gray circles) and 4 μm (green circles) are plotted. The orange circles denote the σ_T^{-1} values obtained from the simulations [shown in (c)].

decreased down to 30 K. The behavior perfectly resembles the simulation shown in Fig. 5(e), i.e., σ_T is almost constant while σ_B shows upon cooling a stronger change.

The quasi-1D regime is highlighted in Fig. 6(b). Compared to the measurement at 300 K, the slope of the $R(s)$ measurement, is gradually increasing and has approximately doubled for the 30 K measurement, i.e., the conductivity at 30 K amounts to $\sigma_T \approx 3 \times 10^5$ S/m. The value for the barrier must be disproportionately smaller compared to the 300 K data in order to shift the 1D range to a length scale that is approximately four times larger. This is qualitatively supported by our finite-element simulations shown as solid lines in Fig. 6(b). The results obtained for σ_T and σ_B are summarized in Fig. 6(c). As obvious, the conductivity of the barrier changes as a function of temperature by an order of magnitude, while the conductivity of the terrace changes only by a factor of 2. An Arrhenius analysis of these data for the terraces results in an activation energy of approximately 1 meV as indicated by the dashed line in Fig. 6(d). The conductivity of the barriers does not show a simple Arrhenius behavior. At 300 K it increases disproportionately, e.g., further channels within the barrier become activated. Considering only the values at lower temperatures, an activation energy of ≈ 40 meV is obtained.

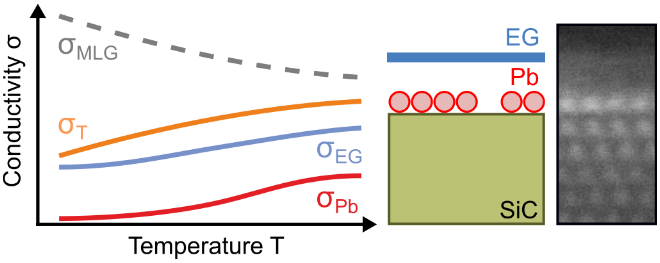

FIG. 7. Schematic drawing of the temperature dependence of the conductivities obtained for MLG and the terrace (σ_T) as well as the estimation of the conductivities σ_{Pb} and σ_{EG} for the Pb and graphene layer. The right part depicts a cross section of the 2D heterostructure on SiC together with a small section from the STEM image in Fig. 1(c).

In the following, we will concentrate on the terrace conductivities and focus on the inherent two transport channels associated with the two layers of Pb and graphene. To start with, we also plotted the resistivity curve deduced from a T-dependent measurement with a larger tip spacing (33 μm). The resistivity values deduced from this measurement are in fact too low due to the parasitic contributions of the barriers. In order to remain in the 1D range and to minimize the impact of terrace inhomogeneities, we carried out collinear resistance measurements in the regime of small distances. The resistivity values determined from temperature-dependent measurements at 4 μm probe spacing are shown in Fig. 6(e). The resistivity decreases with increasing temperature, but the data show some scattering, caused by repeated readjustment compensating thermal drift. We like to mention further that the measurements were started at low temperatures so that drift-related defects tend to increase the resistance over the course of the measurements. The temperature curve shown in Fig. 6(d) therefore represents a worst-case estimate of the resistivity curve. The same trend is found for the resistivities deduced from simulation of the tip-distance-dependent measurements shown in Fig. 6(b) for the different temperatures at the according distances. This is an independent proof and supports overall our conclusions.

As shown in Fig. 6(e), the resistivity decreases gradually by a factor of 2–3 with increasing temperature. For MLG and QFMLG, i.e., hydrogen-intercalated BL structures, the opposite trend is seen, since the remote-phonon scattering rate decreases with decreasing temperature [6,39]. Therefore, this behavior must be caused by the underlying Pb monolayer. For the Pb-intercalated graphene, STEM [cf. Fig. 1(c)] and XSW measurements revealed a distance of 3.7 Å. Therefore, we assume that long-range phonon scattering is not playing a dominant role. This weak coupling is further supported by the charge neutrality of graphene [18,21].

For MLG with an intrinsic doping of $1 \times 10^{13}\,\mathrm{cm}^{-2}$, the conductivity decreases monotonously from around $\sigma_{EG} = 6 \times 10^6$ S/m to around 3×10^6 S/m from 30 K to room temperature, respectively, as sketched in Fig. 7. The associated mobilities of the charge carriers vary typically between 1000–3000 $\mathrm{cm}^2/\mathrm{Vs}$ [39]. A similar behavior is found for QFMLG [6]. Compared to MLG, the absolute conductivity values for our heterosystem are lower by one order of magnitude, probably due to the finite-size effects and defects for intercalation. Nevertheless, the doping level for Pb-intercalated graphene is at least three orders of magnitude lower [21], thus the mobility should be two orders of magnitude higher, if only graphene is contributing.

By means of photoemission spectroscopy it was shown that the 2D Pb interface layer also provides states at the Fermi energy. In contrast to graphene, the charge carriers in the Pb states are massive fermions. The analysis of the Fermi surface yields a Pb electron concentration in the order of $10^{14}\,\mathrm{cm}^{-2}$, i.e., four orders of magnitude larger compared to the charge carrier concentration of the graphene layer atop [17,18,21]. We showed that the Pb monolayer hosts characteristic atomic-sized defects, similar to structures measured for monolayers of various metal adsorbates on Si substrates. As known from corresponding transport measurements performed on such monolayer systems, the scattering times are in the order of $\approx 1-10$ fs [40], i.e., the mobility within these 2D electron gases are as low as 2–20 $\mathrm{cm}^2/\mathrm{Vs}$ and the conductivity amounts to $\sigma_{Pb} = 1 \times 10^5\,\mathrm{S/m}$ assuming a thickness of the interface layer of 0.2 nm for the free electron gas system. From STM and SEM we have seen (cf. Figs. 1 and 2) that the Pb interface layer is percolated, but reveals also many atomic-sized defects, e.g., grain boundaries. Such grain boundaries act as scattering centers and the resulting mean free path length of the electrons would nicely fit to the average distance of 3 nm in between the grain boundaries. Consequently, the conductivity of the Pb interface layer is reduced with reducing the temperature. A schematic behavior for σ_{Pb} is shown in Fig. 7. The effect of scattering due to Au adatoms on Ag-monolayer phases on Si(111) underlines impressively the role of defects in low-dimensional electron gas systems [41]. In various experiments it was shown that epitaxial graphene on SiC is far less sensitive to defects and shows metal-like behavior, i.e., the conductivity of epitaxial graphene is increasing with decreasing temperature [6,39]. Because of the intercalation pathway, the defect density within the Pb interface layer is larger compared to the defects within the graphene layer where intercalation may take place. Also, atomic-sized defects within the Pb interface layer can be easily bridged by graphene. Moreover, because of the mesoscopic Fermi wavelength of the electrons within the graphene layer, large angle scattering within graphene should be suppressed compared to the propagation within the Pb layer. In the context of previous nanoscale transport measurements done on epitaxial graphene, either a metallic behavior or strong localization was seen [39,42]. Therefore, the decrease of the overall conductivity, discussed in context of Fig. 6, must be due to a change of the band structure of graphene proximitized to Pb monolayer, thus the temperature dependence of the graphene atop the Pb monolayer σ_{EG} should show a rather similar behavior than σ_T (cf. Fig. 7). In our experiments it seems that we see at best the onset of a thermally excited transport contribution, i.e., that the band gap in the graphene will be small.

We like to add that for intercalated Pb-multilayer structures, we found a much larger gap, consistently measured with electronic transport and scanning tunneling spectroscopy as well as confirmed by tight binding calculations [19]. For this phase, we argued that plumbene is formed, which is rotated by around 6.5° with respect to graphene. The apparently small interlayer spacing between Pb and graphene as well as the relative twist breaks effectively the symmetry of the graphene lattice giving rise to an electronic gap. Contrarily, the Pb-monolayer phase is epitaxially (almost) perfectly aligned and showed a large van der Waals gap of around 3.7 Å [21]. The difference between the Pb-monolayer and Pb-multilayer phase is also reflected in STS [19]. In contrast to the intercalated Pb-multilayer phase, the Pb monolayer remains metallic from a spectroscopic point of view, i.e., it has a finite and high density of states at E_F. A band gap opening in graphene, providing a much lower density of states, is therefore *de facto* not measurable.

IV. SUMMARY AND CONCLUSION

In this paper we investigated the conductivity of Pb-intercalated epitaxial monolayer graphene. By combining STM, STEM, SEM, and SPA-LEED, we have demonstrated the formation of a close-packed Pb-monolayer structure on both microscopic and macroscopic scales. Nevertheless, the intercalation is accompanied by imperfections that complicated the analysis of transport measurements. While an intercalation rate of approximately 95% was detected on the intercalated terraces, the substrate steps acted as barriers and some of the terraces could not be intercalated at all.

Our measurements showed that, in the case of inhomogeneous or inhomogeneously anisotropic samples, transport measurements on large(r) scales can easily provide underestimated conductivity values. But the conductance measurements can be correctly converted in combination with simulations. Nevertheless, the simulation, in turn, uses approximated real structures, which must be determined beforehand using microscopic methods. The transport signatures introduced by the local inhomogeneities were nicely reproduced by our finite-element simulations. Alternatively, we showed that in the case of quasi-insulating barriers, local transport measurements, e.g., with a four-tip STM, allow the determination of correct conductivities by considering appropriate correction factors known for homogeneous systems.

With this in mind, we determined the conductivity of the graphene/Pb 2D heterosystem, which amounts to $(7 \pm 1) \times 10^5\,\mathrm{S/m}$ at room temperature. Assuming that the free-standing graphene has fewer defects than the intercalated Pb layer itself, the conductivity of the quasineutral graphene should be greater than that of the 2D Pb layer. Moreover, the electrons in graphene should be less sensitive to atomic-sized defects because of the mesoscopic Fermi wavelength. The temperature-dependent measurements showed that the barrier becomes more insulating with decreasing temperature and that hopping with an average activation energy of approx. 40 meV takes place. The conductivity of the terrace, i.e., the intrinsic EG/Pb heterosystem, only decreases marginally and is at our lowest temperature values not switched completely into an insulating state.

In general, the metallic character of this epitaxial 2D heterostructure is confirmed by scanning tunneling and photoemission spectroscopy [18,21]. Nevertheless, based on the considerations above, the decrease of the conductivity in graphene at low temperatures can be explained only by assuming a proximity effect due the Pb-interface structure. Since we have not found any gap openings in spectroscopy and detect most likely only the onset of a SOC-induced band gap opening, we conclude that a gap is in the order of 1–5 meV. Spin-resolved photoemission together with nanoscopic transport measurements at even lower temperatures can hopefully provide further evidence towards the proximity-induced spin-orbit coupling in epitaxial graphene by intercalation of Pb. For epitaxial graphene on Pb/Ir(111) surface a spin-orbit gap of 200 meV was reported [26]. In contrast to this system, which also suggests a much stronger hybridization with the substrate due to the doping of the graphene, the distance between the graphene and the 2D Pb interface is very large at 3.7 Å. Thus, the proposed tunneling processes [27] between the two layers or hybridization schemes with the Pb wave functions [28] are expected to be rather weak. Therefore, our findings are compatible with the assumption of a gap opening due to proximity-induced spin-orbit coupling. However, further low-temperature measurements are necessary in order to quantify the origin further.

ACKNOWLEDGMENTS

We gratefully acknowledge financial support from the DFG through Project Te386/22-1 within FOR5242. We thank also JEOL GmbH for providing us the STEM images obtained during a test measurement. We acknowledge Peter Richter for providing us buffer layer samples and Dr. Zamin Mamiyev for performing SPA-LEED measurements.

---

[1] K. S. Novoselov, A. K. Geim, S. V. Morozov, D. Jiang, M. I. Katsnelson, I. V. Grigorieva, S. V. Dubonos, and A. A. Firsov, Two-dimensional gas of massless Dirac fermions in graphene, Nature (London) **438**, 197 (2005).

[2] A. H. Castro Neto, F. Guinea, N. M. R. Peres, K. S. Novoselov, and A. K. Geim, The electronic properties of graphene, Rev. Mod. Phys. **81**, 109 (2009).

[3] C. Li, Y.-F. Zhao, A. Vera, O. Lesser, H. Yi, S. Kumari, Z. Yan, C. Dong, T. Bowen, K. Wang, H. Wang *et al.*, Proximity-induced superconductivity in epitaxial topological insulator/graphene/gallium heterostructures, Nat. Mater. **22**, 570 (2023).

[4] C. Berger and W. A. de Heer, Flat and safe under the graphene sheet, Nat. Mater. **19**, 583 (2020).

[5] C. Riedl, C. Coletti, T. Iwasaki, A. A. Zakharov, and U. Starke, Quasi-free-standing epitaxial graphene on SiC obtained by hydrogen intercalation, Phys. Rev. Lett. **103**, 246804 (2009).

[6] F. Speck, J. Jobst, F. Fromm, M. Ostler, D. Waldmann, M. Hundhausen, H. B. Weber, and T. Seyller, The quasi-free-standing nature of graphene on H-saturated SiC(0001), Appl. Phys. Lett. **99**, 122106 (2011).

[7] J. Ristein, S. Mammadov, and T. Seyller, Origin of doping in quasi-free-standing graphene on silicon carbide, Phys. Rev. Lett. **108**, 246104 (2012).

[8] J. L. McChesney, A. Bostwick, T. Ohta, T. Seyller, K. Horn, J. González, and E. Rotenberg, Extended van Hove singularity and superconducting instability in doped graphene, Phys. Rev. Lett. **104**, 136803 (2010).

[9] S. Ichinokura, K. Sugawara, A. Takayama, T. Takahashi, and S. Hasegawa, Superconducting calcium-intercalated bilayer graphene, ACS Nano **10**, 2761 (2016).

[10] S. Link, S. Forti, A. Stöhr, K. Küster, M. Rösner, D. Hirschmeier, C. Chen, J. Avila, M. C. Asensio, A. A. Zakharov, T. O. Wehling, A. I. Lichtenstein, M. I. Katsnelson, and U. Starke, Introducing strong correlation effects into graphene by gadolinium intercalation, Phys. Rev. B **100**, 121407(R) (2019).

[11] P. Rosenzweig, H. Karakachian, S. Link, K. Küster, and U. Starke, Tuning the doping level of graphene in the vicinity of the van Hove singularity via ytterbium intercalation, Phys. Rev. B **100**, 035445 (2019).

[12] P. Rosenzweig, H. Karakachian, D. Marchenko, K. Küster, and U. Starke, Overdoping graphene beyond the van Hove singularity, Phys. Rev. Lett. **125**, 176403 (2020).

[13] A. Yurtsever, J. Onoda, T. Iimori, K. Niki, T. Miyamachi, M. Abe, S. Mizuno, S. Tanaka, F. Komori, and Y. Sugimoto, Effects of Pb intercalation on the structural and electronic properties of epitaxial graphene on SiC, Small **12**, 3956 (2016).

[14] S. Chen, P. A. Thiel, E. Conrad, and M. C. Tringides, Growth and stability of Pb intercalated phases under graphene on SiC, Phys. Rev. Mater. **4**, 124005 (2020).

[15] T. Hu, D. Yang, H. Gao, Y. Li, X. Liu, K. Xu, Q. Xia, and F. Ma, Atomic structure and electronic properties of the intercalated Pb atoms underneath a graphene layer, Carbon **179**, 151 (2021).

[16] J. Wang, M. Kim, L. Chen, K.-M. Ho, M. Tringides, C.-Z. Wang, and S. Wang, Manipulation of electronic property of epitaxial graphene on SiC substrate by Pb intercalation, Phys. Rev. B **103**, 085403 (2021).

[17] M. Gruschwitz, C. Ghosal, T.-H. Shen, S. Wolff, T. Seyller, and C. Tegenkamp, Surface transport properties of Pb-intercalated graphene, Materials **14**, 7706 (2021).

[18] B. Matta, P. Rosenzweig, O. Bolkenbaas, K. Küster, and U. Starke, Momentum microscopy of Pb-intercalated graphene on SiC: Charge neutrality and electronic structure of interfacial Pb, Phys. Rev. Res. **4**, 023250 (2022).

[19] C. Ghosal, M. Gruschwitz, J. Koch, S. Gemming, and C. Tegenkamp, Proximity-induced gap opening by twisted plumbene in epitaxial graphene, Phys. Rev. Lett. **129**, 116802 (2022).

[20] Y. Han, M. Kolmer, M. C. Tringides, and J. W. Evans, Thermodynamics and kinetics of Pb intercalation under graphene on SiC(0001), Carbon **205**, 336 (2023).

[21] P. Schädlich, C. Ghosal, M. Stettner, B. Matta, S. Wolff, F. Schölzel, P. Richter, M. Hutter, A. Haags, S. Wenzel *et al.*, Domain boundary formation within an intercalated Pb monolayer featuring charge-neutral epitaxial graphene, Adv. Mater. Interfaces **10**, 2300471 (2023).

[22] S. Brozzesi, P. Gori, D. S. Koda, F. Bechstedt, and O. Pulci, Thermodynamics and electronic structure of adsorbed and intercalated plumbene in graphene/hexagonal SiC heterostructures, Sci. Rep. **14**, 2947 (2024).

[23] C. Brand, H. Pfnür, G. Landolt, S. Muff, J. H. Dil, T. Das, and C. Tegenkamp, Observation of correlated spin-orbit order in a strongly anisotropic quantum wire system, Nat. Commun. **6**, 8118 (2015).

[24] C. Brand, S. Muff, M. Fanciulli, H. Pfnür, M. C. Tringides, J. H. Dil, and C. Tegenkamp, Spin-resolved band structure of

a densely packed Pb monolayer on Si(111), Phys. Rev. B **96**, 035432 (2017).

[25] T. Zhang, P. Cheng, W.-J. Li, Y.-J. Sun, G. Wang, X.-G. Zhu, K. He, L. Wang, X. Ma, X. Chen *et al.*, Superconductivity in one-atomic-layer metal films grown on Si(111), Nat. Phys. **6**, 104 (2010).

[26] I. I. Klimovskikh, M. M. Otrokov, V. Y. Voroshnin, D. Sostina, L. Petaccia, G. Di Santo, S. Thakur, E. V. Chulkov, and A. M. Shikin, Spin-orbit coupling induced gap in graphene on Pt(111) with intercalated Pb monolayer, ACS Nano **11**, 368 (2017).

[27] C. Weeks, J. Hu, J. Alicea, M. Franz, and R. Wu, Engineering a robust quantum spin Hall state in graphene via adatom deposition, Phys. Rev. X **1**, 021001 (2011).

[28] J. Hu, J. Alicea, R. Wu, and M. Franz, Giant topological insulator gap in graphene with 5*d* adatoms, Phys. Rev. Lett. **109**, 266801 (2012).

[29] M. Kruskopf, K. Pierz, S. Wundrack, R. Stosch, T. Dziomba, C.-C. Kalmbach, A. Müller, J. Baringhaus, C. Tegenkamp, F. J. Ahlers, and H. W. Schumacher, Epitaxial graphene on SiC: Modification of structural and electron transport properties by substrate pretreatment, J. Phys.: Condens. Matter **27**, 185303 (2015).

[30] I. Miccoli, F. Edler, H. Pfnür, and C. Tegenkamp, The 100th anniversary of the four-point probe technique: The role of probe geometries in isotropic and anisotropic systems, J. Phys.: Condens. Matter **27**, 223201 (2015).

[31] M. Kruskopf, D. M. Pakdehi, K. Pierz, S. Wundrack, R. Stosch, T. Dziomba, M. Götz, J. Baringhaus, J. Aprojanz, C. Tegenkamp *et al.*, Comeback of epitaxial graphene for electronics: Large-area growth of bilayer-free graphene on SiC, 2D Mater. **3**, 041002 (2016).

[32] W. Norimatsu and M. Kusunoki, Formation process of graphene on SiC (0001), Phys. E **42**, 691 (2010).

[33] T. T. N. Nguyen, N. de Vries, H. Karakachian, M. Gruschwitz, J. Aprojanz, A. A. Zakharov, C. Polley, T. Balasubramanian, U. Starke, C. F. J. Flipse, and C. Tegenkamp, Topological surface state in epitaxial zigzag graphene nanoribbons, Nano Lett. **21**, 2876 (2021).

[34] F. Edler, I. Miccoli, H. Pfnür, and C. Tegenkamp, Space charge layer effects in silicon studied by in situ surface transport, J. Phys.: Condens. Matter **31**, 214001 (2019).

[35] A. Ferreira da Silva, J. Pernot, S. Contreras, B. E. Sernelius, C. Persson, and J. Camassel, Electrical resistivity and metal-nonmetal transition in *n*-type doped 4*h*-SiC, Phys. Rev. B **74**, 245201 (2006).

[36] T. Kanagawa, R. Hobara, I. Matsuda, T. Tanikawa, A. Natori, and S. Hasegawa, Anisotropy in conductance of a quasi-one-dimensional metallic surface state measured by a square micro-four-point probe method, Phys. Rev. Lett. **91**, 036805 (2003).

[37] I. Matsuda, M. Ueno, T. Hirahara, R. Hobara, H. Morikawa, C. Liu, and S. Hasegawa, Electrical resistance of a monatomic step on a crystal surface, Phys. Rev. Lett. **93**, 236801 (2004).

[38] F. Edler, I. Miccoli, S. Demuth, H. Pfnür, S. Wippermann, A. Lücke, W. G. Schmidt, and C. Tegenkamp, Interwire coupling for $\mathrm{In}(4 \times 1)/\mathrm{Si}(111)$ probed by surface transport, Phys. Rev. B **92**, 085426 (2015).

[39] J. Baringhaus, F. Edler, C. Neumann, C. Stampfer, S. Forti, U. Starke, and C. Tegenkamp, Local transport measurements on epitaxial graphene, Appl. Phys. Lett. **103**, 111604 (2013).

[40] S. Yamazaki, Y. Hosomura, I. Matsuda, R. Hobara, T. Eguchi, Y. Hasegawa, and S. Hasegawa, Metallic transport in a monatomic layer of In on a silicon surface, Phys. Rev. Lett. **106**, 116802 (2011).

[41] C. L. Petersen, F. Grey, I. Shiraki, and S. Hasegawa, Microfour-point probe for studying electronic transport through surface states, Appl. Phys. Lett. **77**, 3782 (2000).

[42] D. Slawig, M. Gruschwitz, and C. Tegenkamp, Strong localization in weakly disordered epitaxial graphene, Surf. Sci. **707**, 121801 (2021).